Thermal, structural and optical properties of magnetic $BiFeO_3$ micron-particles synthesized by coprecipitation method: heterogeneous photocatalysis study under white LED irradiation

E. Abdelkader[1]*, L. Nadjia[2], B. Naceur[2], L. Favier-Teodorescu[3]

[1]Université des Sciences et de la Technologie d'Oran Mohammed Boudiaf, Laboratoire des Sciences, Technologie et Génie des Procédés, BP 1505 El M'naouar 31000 Oran, Algérie

[2]Université des Sciences et de la Technologie d'Oran Mohammed Boudiaf, Laboratoire des Matériaux Inorganiques et Application, BP 1505 El M'naouar 31000 Oran, Algérie

[3]Université de Rennes, Laboratoire de Chimie et Ingénierie des Procédés, UM CNRS 6226, Rennes, France

Abstract

Bismuth ferrite, $BiFeO_3$ (BFO) prepared via a coprecipitation method, was used as an effective photocatalyst for the degradation of methylene blue (MB) using a white light-emitting diode (LED-50 W) lamp. The as-prepared material was characterized by TGA, XRD, SEM-EDX, FTIR, and UV-vis-DRS techniques. The effects of experimental key parameters such as pH, catalyst dosage, initial dye concentration, and calcination temperature were investigated. Results showed that BFO-600 (calcined at 600 °C/3 h) was a rhombohedrally-distorted perovskite oxide with the R3c space group. The average crystal size and band gap energy for BFO-600 were found to be 24.8 nm and 2.1 eV, respectively. Under optimal operating conditions ([MB]=20 $mg.L^{-1}$, BFO-600/dye mass ratio=0.5 $g.L^{-1}$, pH=11, and 25 °C), MB/BFO-600/LED process exhibited an efficient photodegradation (up to 94.4%) within 120 min, much higher than the MB sorption process (MB/BFO-600/dark system, 69.4%) and the MB self-photolysis system (MB/LED, 33.9%). The photocatalytic degradation of MB was found to fit well with the pseudo-first-order kinetic model. Thus, the MB photodegradation was attributed to the generation of reactive radicals such as $^{\bullet}OH$, h^+, H_2O_2, and $MB^{\bullet+}$ via direct heterogeneous photocatalysis and mediated by MB through a self-photosensitization process of MB over BFO-600 NPs.

Keywords: magnetic $BiFeO_3$, methylene blue, vis-LED, photocatalysis, photosensitization process.

INTRODUCTION

The perovskite-type oxides have the general formula of ABX_3, where A and B are two cations of different sizes (the A cation much larger than B); X is the anion that bonds to the cations. The ideal ABX_3 perovskite has cubic symmetry with space group Pm3m, where B cation is a 6-fold coordinated to the oxygen anions and A cation is a 12-fold cubo-octahedral coordinated/surrounded by an octahedron of X anions. In the ABX_3 structure, the A cation is normally an alkali or alkaline earth metal or a rare earth element, while the B cation is typically a metallic transition-metal element. The ABX_3 perovskite exhibits lattice distortions that result in the transformation of crystal phases in the following sequence: orthogonal, tetragonal, monoclinic, and triclinic phases. The different degrees of tilting result in different electronic and optical properties [1]. An extensive range of perovskite photocatalyst groups has been developed in the last years for water splitting, carbon dioxide reduction reactions, and organic pollutant degradation under UV or visible light irradiation including: i) titanates: $SrTiO_3$, $BaTiO_3$, $CaTiO_3$, $CoTiO_3$, $NiTiO_3$, $FeTiO_3$, $CdTiO_3$, $PbTiO_3$; ii) tantalates: $NaTaO_3$, $AgTaO_3$, $KTaO_3$, $LiTaO_3$; iii) niobates: $KNbO_3$, $AgNbO_3$, $NaNbO_3$; iv) ferrites: $LaFeO_3$, $GdFeO_3$, $LnFeO_3$ (Ln= Pr, Y), $SrFeO_3$, $GaFeO_3$; and iv) others perovskites such as $BaZrO_3$, $BaCeO_3$, $LaCaO_3$, $LaNiO_3$, $LaCoO_3$, $LaNiO_3$, $SrSnO_3$. However, they are large band gap semiconductors with band gap energy typically lying in the range of 3.0-3.8 eV and can only be activated under UV light [2].

Bismuth-based materials have received special interest due to their particular electronic structure formed by hybrid orbitals of O2p and Bi6s, where the high dispersion of Bi6s orbitals facilitates the charge mobility and the reduction of the band gap. Magnetic $BiFeO_3$, known as the most common multiferroic material in magnetoelectric applications (thin-film capacitor, nonvolatile memory, nonlinear optics, data storage as well as spintronic), has potential use in photoelectrochemical cells and photocatalysis processes [3-5]. These materials show the simultaneous existence of ferroelectric as well as ferromagnetic properties in a single phase at room temperature. In such materials, it is possible to control the magnetization by an applied electric field and vice-versa; this phenomenon is also called of magneto-electric effect [6, 7]. Perovskite-type $BiFeO_3$ shows some physical properties such as high ferroelectric Curie temperature Tc=1100 K, high Néel temperature T_N=650 K, large spontaneous polarization of order of 10-100 $\mu C/cm^2$ in the crystallographic direction [8], low resistivity ($\sigma \sim 10^{-10}$ Ω/cm) mainly caused by the existence of Fe^{2+} and oxygen deficiency, and it exhibits G-type canted antiferromagnetic ordering with

**abdelkader.elaziouti@univ-usto.dz*

https://orcid.org/0000-0002-0078-4816

a cycloid frequency of ~62 nm [9]. The lone pair electron at the 6s shell of Bi is considered the main reason behind the observed ferroelectricity on $BiFeO_3$ while the partially filled 3d shell of Fe is responsible for the canted antiferromagnetic ordering. Magnetic $BiFeO_3$ is widely investigated as a visible light photocatalyst for water splitting and degradation of organic pollutants due to their: i) structural simplicity and flexibility; ii) multiferroic behavior at room temperature; iii) small band gap energy (2.2 eV); iii) high chemical stability; and iv) efficient photocatalytic performance. With these exclusive properties, $BiFeO_3$ (BFO) is identified also as a potential material in solar and fuel cell applications. However, the photocatalytic activity of $BiFeO_3$ is still restricted due to the fast recombination of electron and holes charge carriers. In the past few years, numerous attempts have been devoted to designing and developing the promising performances of visible-light active photocatalysts with a narrower band gap. BFO nanoparticles (NPs) have been synthesized by variety of low temperature wet chemical methods such as hydrothermal [10], coprecipitation [11], sol-gel [12], sonochemical and microemulsion [13], combustion synthesis [14], molten-salt [15], thermal decomposition [16], sol-gel [17], and acid-assisted gel [18, 19] methods.

The use of conventional ultraviolet and visible light sources is recognized to be effective in water splitting and mineralizing of organics pollutants. However, these light sources face various challenges and limitations including relatively high energy consumption, hazardous mercury, require cooling, have a relatively short life-span (<12000 h), the geometry and the size of the light source constrain the design of photocatalytic reactors, low energy efficiency, fragility, and can be difficult to operate. To overcome these shortcomings, great efforts have been made to develop alternative ultraviolet and visible light sources as a major concern in designing compact photoreactors for photocatalysis applications in both gas and liquid phases. In this context, recently new generation energy-efficient light sources such as ultraviolet LED (UV-LED) and visible LED (vis-LED) have been designed and opened a new horizon for a wide range of lighting applications such as heterogeneous photocatalysis. In general, light-emitting diodes (LEDs) are semiconductor-based light sources, which emit photons of different energy (infrared, visible, or near-ultraviolet) in a narrow spectrum based on the electroluminescence effect. The semiconducting material of the LED defines the energy of the induced photons, which can be tuned for a specific photocatalyst. There are various benefits of UV- and vis-LEDs technologies over the traditional ultraviolet and visible light irradiation sources. They are small in size, non-toxic, relatively long life span (more than 50000 h), can operate on a direct current, offer good linearity of the emitted light intensity with electrical current and provide a large degree of freedom in the design of various types of photoreactors. The photocatalytic process under irradiation of LEDs has been primarily performed using UV-LEDs. Conversely, some investigations have reported the feasibility of vis-LEDs as a new paradigm for photocatalytic applications [20-24].

In this research, BFO NPs have been synthesized and designed via the glacial acetic acid-assisted coprecipitation-calcination method and characterized by TGA, XRD, SEM-EDX, FTIR, and UV-vis-DRS techniques. The photocatalytic efficiency of the as-synthesized $BiFeO_3$ catalysts was assessed for the first time by the white vis-LED-light-initiated degradation of blue cationic thiazine dye (methylene blue - MB). The effects of experimental key parameters such as pH solution, catalyst dosage, initial concentration of dye, and calcination temperature on the photodegradation efficiency of the MB over the BFO system were investigated in detail. The mechanism of photocatalytic environmental pollutant degradation application using white LEDs has been highlighted.

EXPERIMENTAL

Materials: $Bi(NO_3)_3.5H_2O$ (≥98.0%, AR), $Fe(NO_3)_3.9H_2O$ (≥98.0%, AR), glacial acetic acid CH_3COOH (AR), NH_4OH (≥99.0%, AR), and methylene blue ($C_{16}H_{18}ClN_3S$, ≥99.0%, AR), all were from Sigma-Aldrich and used without any further purification.

Preparation of BFO NPs: BFO NPs were elaborated by glacial acetic acid-assisted coprecipitation-calcination route using a stoichiometric amount of bismuth nitrate pentahydrate [$Bi(NO_3)_3.5H_2O$], which was dissolved in an appropriate amount of glacial acetic acid (CH_3COOH) stirred at 25 °C for 1 h. Then, a stoichiometric amount of iron nitrate nonahydrate [$Fe(NO_3)_3.9H_2O$] was added to the previous solution. The pH of the resulting solution was adjusted to pH 10 by ammonium hydroxide. Afterward, the solution was continuously stirred at 25 °C for 24 h to form the sol. This sol was heated to 100 °C for 24 h to obtain the xerogel BFO-100 and then calcined at 500, 600, and 700 °C for 3 h in the air to form BFO-500, BFO-600, and BFO-700 powders, respectively.

Characterization: thermogravimetry (TGA) curve was recorded through a thermal analyzer (SDT Q600 V8.2 Build 100, TA Instrum.). Annealing of the samples was carried in a controlled muffle furnace (A-550, Vulcan). Scanning electron microscopy (SEM) coupled with energy-dispersive X-ray spectroscopy (EDX) was carried out by using a microscope (JSM-6490A, Jeol). X-ray diffraction (XRD) analysis was done using a diffractometer (X'Pert PRO 3040/60, Philips). Fourie transform infrared (FTIR) spectra were recorded with a spectrometer (IR, Shimadzu). The optical absorption spectrum was recorded with a UV-visible diffuse reflectance spectrophotometer (UV-vis-DRS, 750, Jasco). All UV-visible spectra were measured with a spectrophotometer (Dual Beam 60, Cary) in the range of 400-800 nm, using deionized water as a reference.

Photocatalytic activity experiments: the photocatalytic performance of the as-synthesized BFO photocatalyst was assessed by the degradation of methylene blue (MB) solution using a 50 W warm white light LED lamp irradiation, as the visible light source. In a typical assay, 0.1 g of the photocatalyst was added to 100 mL of MB at 10 $mg.L^{-1}$ in a Pyrex vessel under constant magnetic stirring. The solution

pH was adjusted to 11 by adding NaOH. The suspension was stirred for 60 min in a dark condition to attain the adsorption/desorption equilibrium, then the solution was subjected to white LED irradiation under continuous stirring. Afterward, at regular time intervals, 4 mL of suspension was collected, the solid phase was separated from the suspension using centrifugation at 3000 rpm for 15 min, and the concentrations of the resulting solutions were then monitored with a spectrophotometer (Dual Beam 60, Cary).

RESULTS AND DISCUSSION

TGA analysis: the thermal decomposition of the as-synthesized BFO-100 powder was analyzed using TGA. Based on the TGA curve in Fig. 1, BFO-100 powder displayed three well-defined events of weight loss. The first weight loss of 23.85% was observed in the temperature range of 25-200 °C, indicating the evaporation of moisture and glacial acetic acid (boiling point= 118-119 °C) from the BFO-100 surface. In the range of 200-450 °C, the second sequential weight loss of 20.17% was ascribed to the volatile fractions like nitrate group, C-group, OH group, and water. The last weight loss (23.99%) occurred between 450 and 1000 °C. The formation of BFO occurred between 450 and 650 °C. At temperatures higher than 650 °C, a change to a higher oxidation state from ferrous to ferric led to a gain in weight. Transitions to the non-equilibrium decomposition of BFO at 920 °C corresponded to the β→γ transition of BFO. This transition is not thermodynamically intrinsic. Therefore, the calcination temperature was limited to 600 °C to investigate the formation of the BFO phase [25]. The thermal decomposition stages of BFO are displayed in Table I.

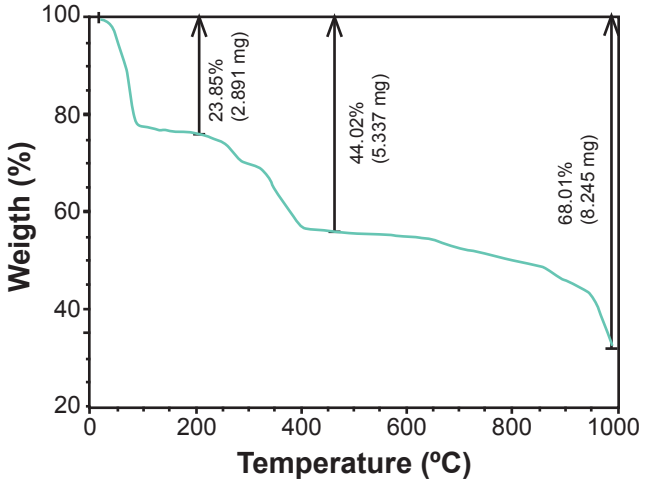

Figure 1: TGA curve of the xerogel (BFO-100).

Table I - Thermal decomposition stages of BFO.

Temperature interval (°C)	25-200	200-450	450-1000	Total
Weight loss (%)	23.85	20.17	23.99	68.01

XRD analysis: the XRD pattern of calcinated powder at 600 °C/3 h is depicted in Fig. 2. The diffraction peaks of BFO-600 at 2θ= 22.665°, 32.000°, 32.315°, 39.715°, 45.988°, 51.526°, 57.189°, and 67.296° can be indexed as (012), (104), (110), (006), (024), (116), (214), and (220) planes of rhombohedrally-distorted perovskite $BiFeO_3$ phase, which crystallizes in R3c space group symmetry (JCPDS file 01-073-0548). The slight splitting of peak around 2θ=32° to double peaks (104)/(110) from the BFO-600 are shown in the inset of Fig. 2, confirming the rhombohedral symmetry of BFO. Supplementary peaks can be attributed to the higher local calcination temperature such as $Bi_2Fe_4O_9$ and the evaporation of volatile phases, such as Bi_2O_3.

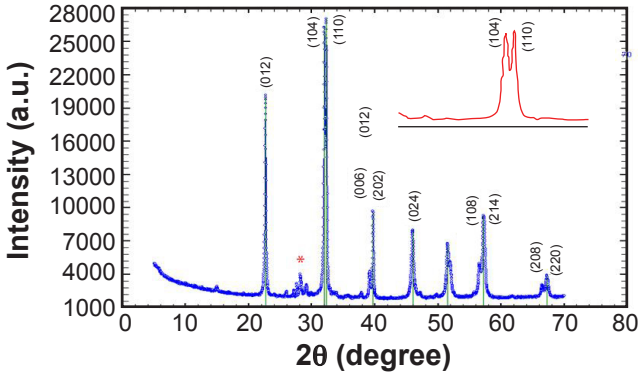

Figure 2: XRD patterns of the BFO-600 NPs powder (inset: the magnified peak in the ranges of 2θ from 30 to 33°; *-impurities such as $Bi_2Fe_4O_9$ and/or Bi_2O_3).

Average crystallite size (D_{XRD}): D_{XRD} of perovskite BFO-600 is predicted by Scherrer's formula [26]:

$$D_{XRD} = \frac{K.\lambda}{\beta.\cos\theta} \quad (A)$$

where λ is the X-ray wavelength (0.15406 nm), θ is the Bragg angle, β is the full width at half maximum (FWHM) of the most intense peak, and K is the crystallite-shape factor (K ~0.89). The average crystal size of perovskite BFO-600 was estimated to be 24.8 nm. *Specific surface area (SSA)*: assuming that the $BiFeO_3$ NPs have a spherical shape and uniform size, the SSA can be estimated by BET equation [27]:

$$SSA = \frac{6000}{\rho.D_{XRD}} \quad (B)$$

where D_{XRD} is the average particle size in nm and ϱ is the theoretical density of $BiFeO_3$ (8.35 $g.cm^{-3}$). As shown in Table II, the specific surface area (SSA) value of BFO-600 was found to be 20.9 $m^2.g^{-1}$. The physical properties of the system BFO-600 are impacted by the crystal stress (S). Therefore, S was assessed by using the following formula [28]:

$$S = \frac{\beta.\cos\theta}{4} \quad (C)$$

Table II - Crystallographic parameters of BFO-600 NPs catalyst.

Catalyst	2θ (degree)	FWHM (degree)	D_{XRD} (nm)	D_t ($g.cm^{-3}$)	SSA ($m^2.g^{-1}$)	S	γ x10^{17} (line/m^2)	ε
$BiFeO_3$	32	0.333	24.87	8.35	20.94	0.0694	1.6167	0.0714

Dislocation density (γ): γ is a measure of the number of dislocations in a unit volume of a crystalline material i.e. the length of dislocation lines per unit volume of the crystal (m/m^3). Edge and screw dislocations distort a crystal lattice, causing elastic stress around the dislocation line, and hence strain energy. For ultimate strength, dislocations must be eliminated. The dislocation density was calculated from:

$$\gamma = \frac{1}{D_{XRD}^{\ 2}} \qquad (D)$$

Since dislocation density and strain are the indications of the dislocation network in the matrix, a higher value of dislocation density indicates the formation of high-quality crystals. However, a lower value of dislocation density for composite indicates disorder existing in the system. *Microstrain (ε)*: ε was assessed from the following formula:

$$\varepsilon = \frac{\beta}{4 \tan \theta} \qquad (E)$$

In general, the micro-strain in nano-crystallites is caused by several factors, like non-uniform lattice distortions, dislocations, antiphase domain boundaries, grain surface relaxation, etc. In $BiFeO_3$, the most common defects such as oxygen vacancies are major contributions to the micro-strain; these oxygen vacancies are reportedly at a lower energy level than the adjacent Fe 3d levels, resulting in sub-band gap defect states. Another contribution to the micro-strain comes from the unsaturated bonds on the surface of the nanoparticles, which create deep and shallow defect levels within the band gap helping to stabilize other valence states for the cations, as Fe^{2+}, or adsorbed molecules, such as FeOOH [29, 30]. Both effects (Fe^{2+} and FeOOH

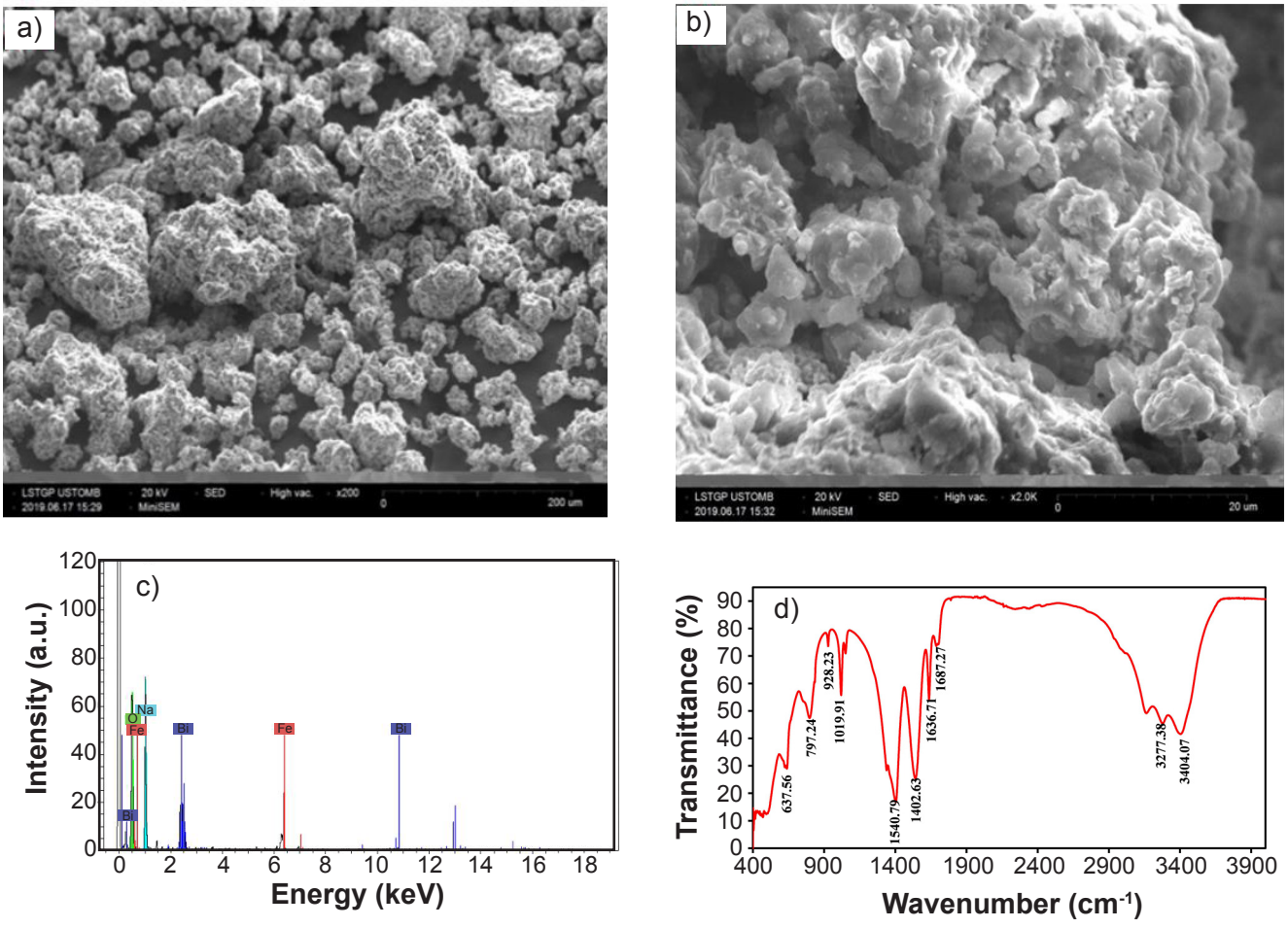

Figure 3: SEM images showing the morphology of BFO-600 NPs at low (a) and high magnification (b), EDX spectrum (c), and FTIR spectrum (d) of BFO-600 NPs.

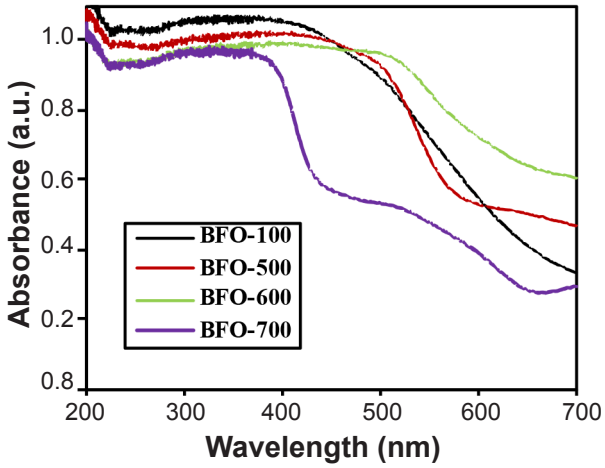

Figure 4: UV-vis-DRS absorption spectra of the BFO calcined at various temperatures.

stabilization) may differently affect the photocatalytic properties. In the present paper, we expect that a reason for the supermetallic behavior is the high strain ε in the dislocation core, which exceeds ε=7% resulting in local modifications of the band structure and carrier mobility. The structural parameters, crystallite size, specific surface area, crystal stress, dislocation density, and microstrain of BFO-600 NPs are tabulated in Table II.

SEM-EDX analysis: the morphology of BFO-600 NPs was observed by scanning electron microscopy (SEM) as shown in Fig. 3. At low magnification (Fig. 3a), the BFO-600 NPs were not identifiable. On a higher magnification (Fig. 3b), BFO-600 NPs tended to aggregate to form bigger particles. NPs' agglomerates were prominently visible. The elemental analysis of the BFO-600 sample was carried out by energy dispersive X-ray analysis (EDX), as depicted in Fig. 3c. The EDX plot indicated the composition of elements present in the BFO-600 catalyst in terms of the $BiFeO_3$. BFO-600 sample showed the exact match for standard peak position for Bi, Fe, and O. An extra peak related to the Na atom was observed in the EDX plot due to the presence of salt excess in the BFO-600 matrix.

FTIR analysis: FTIR spectrum of the as-prepared BFO-600 NPs is displayed in Fig. 3d. The bands at about 450 and 550 cm^{-1} were assigned to the Fe-O stretching and bending vibrations of the octahedral FeO_6 groups in the perovskite-type structure, respectively. Furthermore, the broad bands appeared at 3404.07 and 1636.71/1687.27 cm^{-1}, which were related to the bending and stretching vibrations of the water molecules absorbed by the sample. The other bands at 797.24 and 928.23 cm^{-1} were attributed to the BFO-600 NPs. The bands at 1019.16 and 1402.63 cm^{-1} were ascribed to the stretching vibrations of C=O and C-C, respectively, which appeared due to absorption of carbon during the exposure of the sample to air [31].

UV-vis-DRS analysis: the band structure of $BiFeO_3$ is sensitive to external factors, such as temperature and stress. The obvious metal-insulator transition of $BiFeO_3$ NPs was confirmed by investigating the variation of band gap value as a function of temperature. Fig. 4 illustrates UV-vis absorption spectra of BFO NPs with various calcination temperatures. A gradual red-shift of the absorption band edge of BFO materials with increasing calcination temperature up to 600 °C may be explained by the presence of defect-induced energy levels between conduction (CB) and valence (VB) bands, more specifically energy levels close to the conduction band [32]. These shallow defect levels (oxygen vacancy) can reduce the effective band gap for higher temperatures if their dislocation density is high enough, allowing the excitation of electrons from VB to CB with the absorption of relatively low energy photons and would be helpful for the significantly enhanced photocatalytic performance of the BFO catalyst. The absorption edge of BFO-100 at 539.13 nm red-shifted to 551.11 nm for BFO-500 and 590.47 nm for BFO-600.

Conversely, as displayed in Table III, the calcination of BFO at 700 °C induced a blue-shift of the absorption band edge indicating an increase in the band gap energy as a result of a reduction of the concentration of defects in local lattice and the strengthening of the quantum confinement effect. Thus, the blue shift to shorter wavelengths could be attributed possibly to a change in the electronic band structure owing to the quantum confinement effect [33]. It can also be seen from the tabulated data, as displayed in Table III, that the increase in the calcination temperature of BFO up to 600 °C significantly enhanced visible light absorption intensity (λ≥500 nm). However, at 700 °C, a scale decline in the visible light absorption intensity was

Table III - Optical and electronic properties of BFO calcined at various temperatures.

Catalyst	E_g (eV)	λ (nm)	χ (eV)	E_{VB} (eV)	E_{CB} (eV)	LUMO (eV)	HOMO (eV)
BFO-100	2.30	539.13	5.89	2.54	0.24	-	-
BFO-500	2.25	551.11		2.52	0.27	-	-
BFO-600	2.10	590.47		2.44	0.34	-	-
BFO-700	2.95	420.33		2.87	-0.08	-	-
MB dye	1.87	664.00	-	-	-	-0.6	1.27

LUMO: lowest unoccupied molecular orbital; HOMO: highest occupied molecular orbital.

observed for BFO-700 possibly attributed to the presence of Bi_2O_3 and $Bi_2Fe_4O_9$ as secondary phases, as confirmed via TGA observations, acting as a recombination center for charge carriers.

As shown in Fig. 5, the band gap energy can be calculated by the Kubelka-Munk theory (Eqs. F and G) [34]:

$$\alpha \cong \frac{(1 - R^2)}{2R} \quad (F)$$

$$R \cong 10^{-A} \quad (G)$$

where R is the reflectance and A is the absorbance. Tauc's equation (Eq. H) [35] has been used to get the band gap value for various calcination temperatures:

$$(\alpha.h\nu)^{1/n} = \beta\,(h\nu - Eg) \quad (H)$$

where α, hν, E_g, β, and n are absorption coefficient, photon energy, band gap energy, and a proportional constant, respectively. The value of the exponent n denotes the type of the sample transition. For a direct allowed transition, n=½, and for an indirect allowed transition, n=2. Generally, the direct allowed transition has been reported for $BiFeO_3$; so, n=½ was used in this work. $BiFeO_3$ is recognized to have a band gap of 2.1 to 2.7 eV in a different form of the material such as bulk, nanomaterial, or single crystalline material [36]. Thus, in the actual experiment, the relational expression becomes:

$$(\alpha.h\nu)^2 = A\,(h\nu - Eg) \quad (I)$$

By extrapolating the linear portion of $(\alpha.h\nu)^2$ against hν plot to the point $(\alpha.h\nu)^2=0$, the corresponding band gap energy was about 2.3, 2.25, 2.1, and 2.95 eV for BFO-100, BFO-500, BFO-600, and BFO-700, respectively. Based on the above results, BFO-600 NPs exhibited low band energy in comparison with other explored catalysts (BFO-100, BFO-500, and BFO-700) and a strong potential application

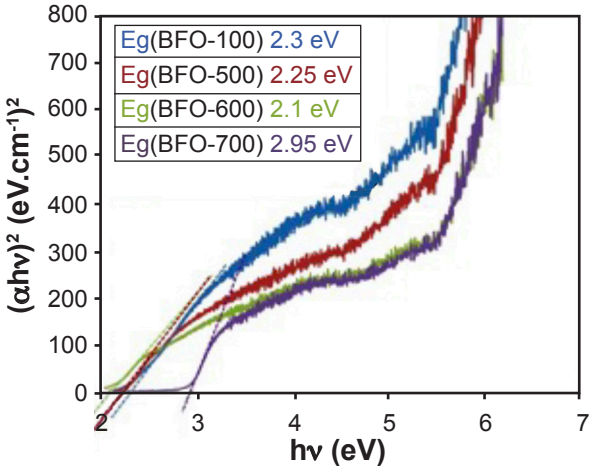

Figure 5: Plot of $(\alpha.h\nu)^2$ vs. (hν) of BFO calcined at various temperatures.

as an appropriate photocatalyst for the degradation of materials in the visible region. The potentials of the conduction band (CB) and valence band (VB) edges of BFO calcined at various temperatures were assessed according to the Mulliken electronegativity theory [37], as shown in Eqs. J and K:

$$E_{VB} = \chi - E_e + 0.5E_g \quad (J)$$

$$E_{CB} = E_{VB} - E_g \quad (K)$$

where χ is the absolute electronegativity of the semiconductor, which is the geometric mean of the electronegativity of the constituent atoms. Herein, the electronegativity of an atom is the arithmetic mean of the atomic electron affinity and the first ionization energy; E_e is the scaling factor relating the hydrogen electrode scale, NHE, to absolute vacuum scale, AVS (4.5 eV vs. AVS for 0 V vs. NHE), and E_g is the band gap of the semiconductor; E_{CB} and E_{VB} stand for the CB and VB edge energy, respectively. For $BiFeO_3$, the χ value was calculated to be 5.85 eV for BFO. The E_{VB} and E_{CB} were estimated to be 2.54 and 0.24 eV for BFO-100, 2.52 and 0.27 eV for BFO-500, 2.44 and 0.34 eV for BFO-600, and 2.87 and -0.08 eV for BFO-700, respectively. The calculated CB and VB potentials of BFO catalysts and the theoretical LUMO and HOMO values of MB dye are reported in Table III.

Effect of pH on the photolysis of methylene blue (MB): the effect of pH solution on the direct photolysis of MB dye under white light (50 W) LED irradiation was explored at various pH mediums from 3 to 11, as shown in Figs. 6 and 7a. The experimental data plot (absorbance vs. time, Fig. 6) showed that MB self-photolysis was nearly independent of the pH with the non-negligible degradation efficiency in all selected pH mediums. 42.7%, 37.5%, and 33.8% were found for pH 3, 6, and 11, respectively, within 120 min exposure time, as illustrated in data plot (η vs. pH, Fig. 7a), exhibiting almost similar order of magnitude. The relatively slow degradation of MB was observed in acidic media (i.e. pH=3-6), while an alkali medium (i.e. pH=11) induced a higher kinetic rate. In basic aqueous solutions under white LED-50 W irradiations, highly reactive hydroxyl radicals can be formed through monoelectronic reduction of MB^+ by the hydroxyl ion:

$$MB^+ + OH^- \rightarrow MB^{\bullet} + {}^{\bullet}OH \quad (L)$$

and hydroxyl radical species can react with each other producing H_2O_2, which is an important active specie in degradation processes:

$$2{}^{\bullet}OH \rightarrow H_2O_2 \quad (M)$$

then, oxygen as a radical scavenger can react with $MB^{\bullet}$ radical and form $O_2^{\bullet}$ as another important intermediate specie according to the reaction:

$$MB^{\bullet} + O_2 \rightarrow MB^{+} + O_2^{-\bullet} \quad (N)$$

Thus, the photolysis of MB at basic media could be preceded via direct reactions of MB with highly reactive radical species that are formed in the presence of sunlight irradiation. In acidic conditions, H^+ ions are too high in concentration and the oxidation of H_2O and OH^- into $^{\bullet}OH$ radicals via the white LED-50 W excitations is suppressed due to an excessive concentration of H^+ and a low concentration of OH^-, indicating that excitation of dye molecules by photon and then dispersion of their excitation energy had no role on the decolorization of the dye and $^{\bullet}OH$ radicals were not part of the degradation process:

$$O_2^{-\bullet} + H^+ \rightarrow {}^{\bullet}HO_2 \quad (O)$$

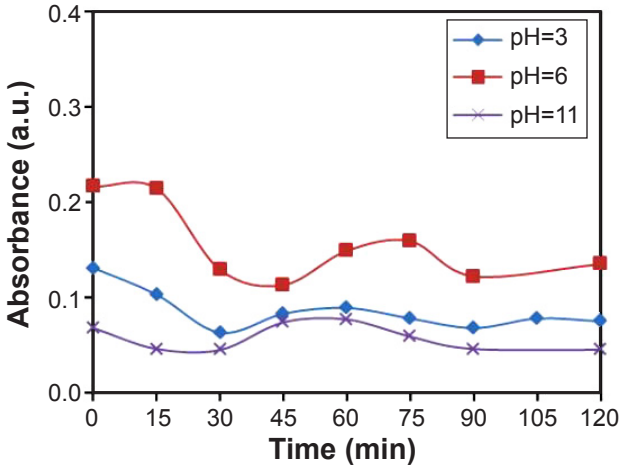

Figure 6: Effect of pH solution on the direct photolysis of MB under 50 W white light LED irradiation

Furthermore, when the pH exceeds the pKa=4.88, the reaction in Eq. O proceeds inversely and, thus, is inhibited. As a result, there are less $^{\bullet}HO_2$ radicals, which are lower in redox potential and oxidizing capacity in the reaction system. Furthermore, the lack of $^{\bullet}HO_2$ radicals suppresses Eqs. P to R and these reactions also inhibit oxidation, as they produce oxidizing substances lower in oxidizability:

$$^{\bullet}HO_2 + {}^{\bullet}HO_2 \rightarrow H_2O_2 + O_2 \quad (P)$$

$$O_2^{-\bullet} + {}^{\bullet}HO_2 \rightarrow {}^{-}HO_2 + O_2 \quad (Q)$$

$$^{-}HO_2 + H^+ \rightarrow H_2O_2 \quad (R)$$

The slight increase in the degradation efficiency of MB over the pH values in the range of pH between 3 and 6 was attributed to the partial self-association of MB^+ monomers (λ_{MB+}=664 nm) as cationic dimers $(MB^+)_2$ ($\lambda_{(MB+)2}$=624 nm) in face-to-face arrangement to minimize their hydrophobic interaction with water [38].

Effect of pH on the sorption and the photocatalysis processes: the pH of the wastewater is one of the vital parameters that determine the efficiency of the sorption and the photocatalysis processes under LED irradiation. Thus, the experiments were conducted over a range of pH values from 3 to 11 at a fixed dye concentration (10 mg.L^{-1}), catalyst dosage (0.5 g/L of BFO-600), and 25 °C at a contact time of 120 min, and the respective results are illustrated in Fig. 7a. The sorption of MB dye from aqueous solution on BFO-600 was pH-dependent with the maxima sorption efficiency of 46.4%, 71.7%, and 69.4% achieved at pH 3, 6, and 11, respectively, within 60 min [39]. Under LED irradiation, the degradation efficiency decreased from 17.9% to 5.6% as pH was increased from 3 to 6, and then rapidly raised beyond pH=6, almost reaching 94.4% at pH=11. The optimum pH was found to be 11 with the maximum photocatalytic efficiency (up to 94.4%) achieved within 120 min. We assumed that BFO-600, as photocatalyst metal oxide with amphoteric properties, formed metal hydroxyl groups (BFO-600-OH) via the association of H_2O molecules and dissociation of OH^- hydroxyl groups at surface metal sites. The pH of point of zero charge (pH_{PZC}) of the BFO-600 photocatalyst was 2 [40]. At pH<pH_{PZC}, the catalyst surface was positively charged, according to the following reaction:

$$BFO\text{-}600 + H_2O \rightarrow BFO\text{-}600\text{-}H_3O^+ \quad (S)$$

and it was negatively charged at pH>pH_{PZC}, given by the following reaction:

$$BFO\text{-}600 + H_2O \rightarrow BFO\text{-}600\text{-}O^- + OH^- \quad (T)$$

MB is a blue cationic thiazine dye that has two functional groups (i.e. dimethyl amino cations $R\text{-}N(CH_3)_2^+$ and chloride ions Cl^-). Therefore, under a strong acidic medium (i.e. pH=3>pH_{PZC}=2), the adsorption process occurred because of electrostatic attraction between the negatively charged photocatalyst surface (BFO-600-O^-) and the strongly ionized cationic groups of cationic dye $R\text{-}N(CH_3)_2^+$, thereby increasing the sorption efficiency of BFO-600 towards the MB (up to 46.4%), as shown in Eq. U:

$$BFO\text{-}600\text{-}O^- + R\text{-}N(CH_3)_2^+ \rightarrow BFO\text{-}600\text{-}O^-\text{-}R\text{-}N(CH_3)_2^+ \quad (U)$$

At this pH (i.e. pH=3), almost close to pH_{PZC}=2 and according to general colloid chemistry principles, electrostatically stabilized dispersion system typically loses stability when the magnitude (i.e. absolute value) of the zeta potential decreases to less than approximately 30 mV. As a result, there is some region surrounding the condition of zero zeta potential (i.e. pH_{PZC}=2) for which the system is not particularly stable. Within this unstable region, the BFO-600 NPs may agglomerate, thereby increasing the particle size and reducing the negative site of the surface catalyst. As a result, the sorption processes could not be effectively operated at acidic pH conditions (i.e. pH_{PZC}=3). Moreover, when pH solution was increased up to 6 (i.e. pH=6>pH_{PZC}=2), a clear increase in the sorption efficiency

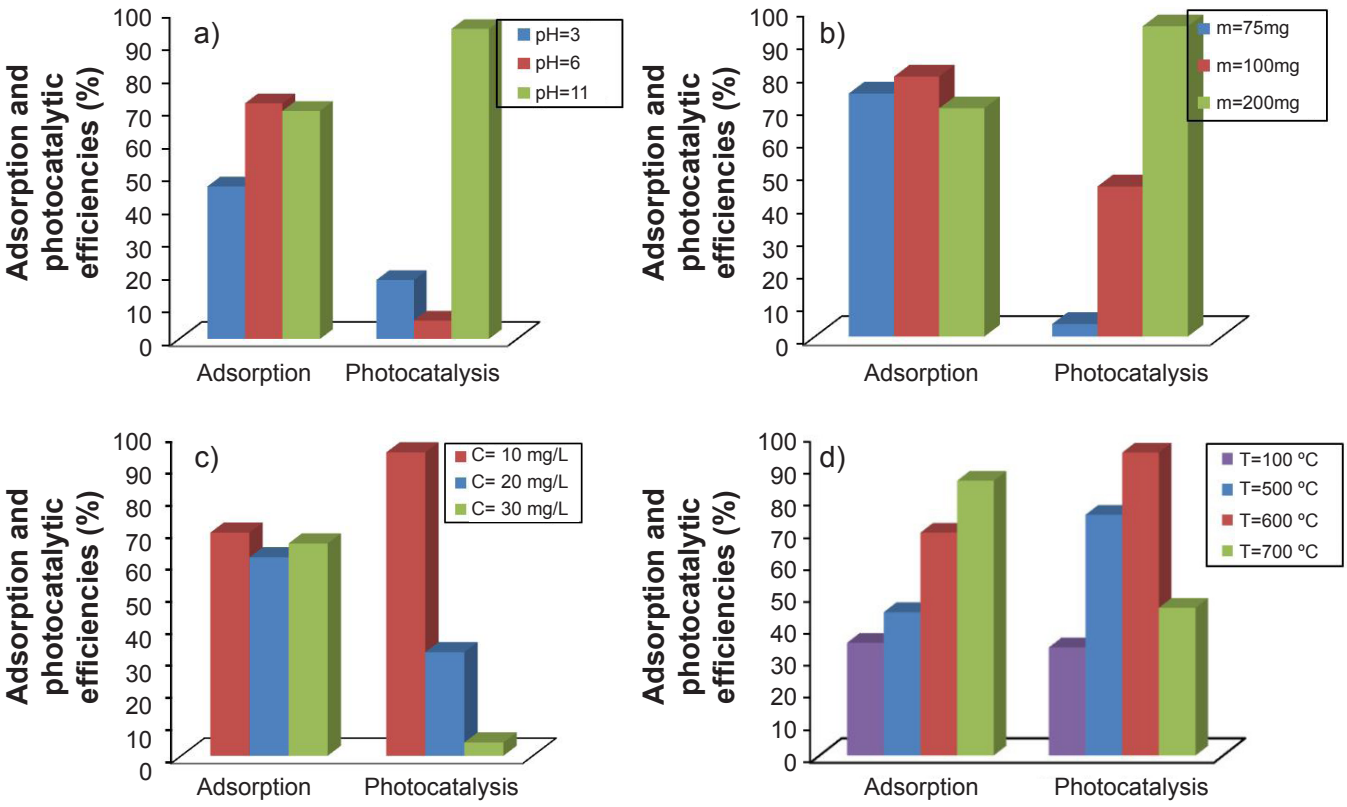

Figure 7: Effect of pH solution (a), catalyst dosage (b), initial concentration of dye (c), and calcination temperature (d) on the sorption and photocatalysis of MB over BFO-600 under 50 W white light LED irradiation.

of MB (up to 71.7%) was observed due to the electrostatic attraction between oppositely charged species. Although electrostatic attraction occurs between the cationic MB molecules {monomers $R\text{-}N(CH_3)_2^+$ (Eq. V) and/or dimers $[R\text{-}N(CH_3)_2^+]_2$} and negatively charged surface of BFO-600 NPs (BFO-600-O^-) at high alkali pH (i.e. pH=11>pH_{PZC}=2), the sorption efficiency of BFO-600 towards the MB remained almost steady (up to 69.4%.) because of: i) the competitive sorption between BFO-600-O^- and $[R\text{-}N(CH_3)_2^+]_2$ (Eq. W) competing with the monomers $R\text{-}N(CH_3)_2^+$ on the dyes for the active sites, thereby decreasing the sorption rate; and ii) the Coulombic repulsion between BFO-600-O^- surface against the OH^- ions (Eq. X), which resulted in the breakage of hydroxylation of the BFO-600 NPs surface.

$$\text{BFO-600-}O^- + R\text{-}N(CH_3)_2^+ \rightarrow \text{BFO-600-O-}R\text{-}N(CH_3)_2 \quad (V)$$

$$2(\text{BFO-600-}O^-) + [R\text{-}N(CH_3)_2^+]_2 \rightarrow (\text{BFO-600-O})_2\text{-}[R\text{-}N(CH_3)]_2 \quad (W)$$

$$\text{BFO-600-}O^- + OH^- \rightarrow \text{BFO-600} + H_2O \quad (X)$$

Based on computation, the photocatalytic efficiency was analogous with previously reported results [41, 42]. The relatively slow degradation observed in acidic media (i.e. pH=3-6) was due to the inhibitive oxidation reaction, which produced oxidizing substances with low redox potential and oxidizability such as •OH and $•HO_2$ radicals. But, with increasing the hydroxyl ions, the rate of photocatalysis was dramatically increased. The basic conditions were crucial for the generation of •OH radicals. We noted that the self-photosensitization of cationic MB adsorbed on negatively charged BFO-600 NPs can also contribute to almost totally the degradation of MB molecules at pH 11.

Effect of the catalyst dosages: the impact of catalyst dosages toward the degradation efficiency of MB by the BFO-600-NPs system was investigated and depicted in Fig. 7b. It can be seen that the degradation process of MB was obviously accelerated along with increasing catalyst dosages. The degradation of MB achieved 3.8% and 45.7% with 0.07 and 0.1 g of catalyst dosage, respectively, and up to 94.4% when the catalyst dosage increased to 0.2 g. This result was possibly assigned to the increased amount of active sites on the BFO-600 catalyst surface, which was expected to produce more oxidizing substances in higher redox potential such as •OH radicals, boosting the reactions of MB degradation [43].

Effect of the initial concentration of MB dye: the initial concentration of MB dye played a key factor in the photocatalytic degradation process. The effect of MB initial concentration on the photocatalytic activity was carried out in the range between 10 and 30 $mg.L^{-1}$ with optimal BFO-600 catalyst dosage (0.2 g in 200 mL of aqueous solution), pH 11, T=25 °C, and reaction time of 120 min. As displayed in Fig. 7c, it was clearly observed that the degradation efficiency of MB was sharply reduced from 94.9% to 4.2% as the MB concentration was increased from 10 to 30

mg.L^{-1}. This finding was probably due to the obstruction of light penetration into the solution medium, meaning that the pathlength of photons inside the solution decreased as a result of the increase in the MB local concentration and the opacity of the solution [44]. Moreover, the initial concentration of MB dye (20 mg.L^{-1}) was slightly effective for MB degradation; the degradation efficiency was about 32.2%, a value similar to that of the photolysis reaction (33.8%). The minimal, optimum concentration of MB (10 mg.L^{-1}) solution was required for better photodegradation efficiency.

Effect of the calcination temperature: temperature is one of the most important environmental factors affecting the photocatalysis processes of aqueous species. The influence of the calcination temperature toward MB degradation by BFO-600 photocatalyst is depicted in Fig. 7d and its corresponding results are summarized in Table IV. The photocatalytic efficiency increased from 33.7% for BFO-100 to 94.4% for BFO-600. However, the further increase in the calcination temperature to 700 °C induced a reduction of the photocatalytic efficiency to 46.0%. So, BFO-600 was considered the best active phase for the degradation of MB dye under vis-LED irradiation. The amorphous phase in nature of BFO-100, as observed in XRD patterns, and many imperfections and defects in BFO-500 acted as recombination centers for the photo-induced electrons and holes, thus, limiting the photodegradation process. At calcination temperature of 700 °C, with the presence of Bi_2O_3 and $Bi_2Fe_4O_9$ as secondary phases, as depicted in TGA and XRD analysis, acted as a recombination center for charge carriers, leading to a degradation decrease. For a better understanding of the influence of calcination temperature on the photocatalytic efficiency, the photocatalytic degradation of MB azo dye was investigated by a pseudo-first-order kinetic model:

$$\ln \frac{C}{C_0} = -K.t \qquad (Y)$$

where C_0 and C are the dye concentrations (mg.L^{-1}) before and after vis-LED irradiation, respectively, k is the pseudo-first-order rate constant (min^{-1}), and t is the reaction time (min). By plotting ln(C/C$_0$) versus irradiation time, t (Fig. 8), the value of the kinetic constant K was assessed by the slope of the straight-line. Based on the rate constant (K_{app}, min^{-1}) as displayed in Table IV, BFO-600 exhibited the best photocatalytic performance (94.4% within 120 min) with the highest value of K (0.0242 min^{-1}). In fact, the rate constant K in different systems increased in the following order: BFO-600 (0.0242 min^{-1}) >BFO-500 (0.0143 min^{-1}) >BFO-100 (0.0133 min^{-1}) >BFO-700 (0.0082 min^{-1}).

Comparative study: Fig. 9 shows a comparative study in dark and under LED irradiation with and without BFO-600

Table IV - Pseudo-first-order kinetic parameters for the photocatalysis of MB over BFO at various calcination temperatures under 50 W white light LED irradiation.

T (°C)	Catalyst	η (%)	η' (%)	K (min^{-1})	$t_{½}$ (min)	R^2
100	BFO-100	35.1	33.7	0.0133	52.11	0.6212
500	BFO-500	44.7	75 0	0.0143	48.47	0.8986
600	BFO-600	69.4	94.4	0.0242	28.64	0.9667
700	BFO-700	85.6	46.0	0.0082	84.53	0.7606

η: adsorption efficiency; η': photocatalytic efficiency.

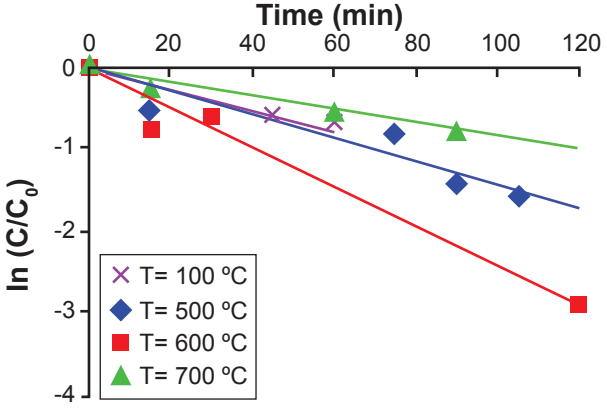

Figure 8: Pseudo-first-order kinetic of the photocatalysis MB over BFO at various calcination temperatures under 50 W white light LED irradiation.

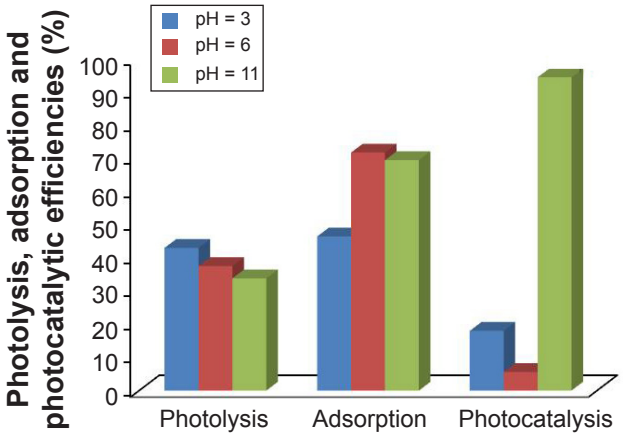

Figure 9: Comparative study in dark and under LED irradiation with and without BFO-600 catalyst.

catalyst at different solution pH. It was found that both the self-photolysis under LED irradiation and the sorption processes showed non-negligible degradation of MB in all selected pH mediums. Whereas, the heterogeneous photocatalysis (under LED irradiation with BFO-600 as a catalyst) exhibited maximum photocatalytic efficiency (up to 94.4%) achieved within 120 min at pH=11.

Mechanism: the photocatalytic efficiency of semi-conductor nanostructured materials is primarily based on the generation of the electron-hole pair when using light energy greater than its band gap energy. The probable mechanism scheme of photocatalytic activity of BFO-600 NPs catalyst on the degradation of MB is shown in Fig. 10. According to the band edge position (Table III), under a white light-emitting diode (LED 50 W) lamp, the energy of the light excitation is sufficient to directly excite the BFO-600 (E_g=2.1 eV). When the LED light falls on the BFO-600 NPs catalyst the electrons (e^-) in the VB get excited and jump onto the CB and then migrate to the particle surface with simultaneous generation of the same amount of holes (h^+) in the VB:

$$BFO\text{-}600 + h\nu_{(LED\text{-}50W)} \rightarrow BFO\text{-}600\ (e^-_{CB} + h^+_{VB}) \qquad (Z)$$

The photogenerated electrons move towards the BFO-600 surface, which acts as a trap and thus inhibits the recombination of photogenerated electron-hole pairs. Because the redox potentials of $O_2/O_2^{\bullet-}$ (-0.33 V/NHE) is slightly more negative, while the redox energy of $O_2/^{\bullet}OH$ (+0.7 V/NHE) is much more positive than the CB edge potential of BFO-600 (+0.34 eV/NHE), the photoinduced electron in the CB cannot reduce O_2 to generate $O_2^{\bullet-}$ but can react with O_2 to produce $^{\bullet}OH$ radical (Eq. AA). Meanwhile, the photogenerated hole (h^+) also moves to the particle surface and can react with surface OH^- groups, which act as donor species to yield $^{\bullet}OH$ (Eq. AB) due to the VB edge energies of BFO-600 (+2.44 eV/NHE) that is more positive than the standard potential of $OH^-/^{\bullet}OH$ (+1.99 eV/NHE):

$$O_{2ads} + 2H_2O + 4e^- \rightarrow 4^{\bullet}OH_{ads} \qquad (AA)$$

$$h^+ + OH^-_{ads} \rightarrow {}^{\bullet}OH_{ads} \qquad (AB)$$

Thus, the generated radicals, as powerful oxidizing agents, attack organic molecules causing the chain cleavage and oxidation reactions of dye molecules by:

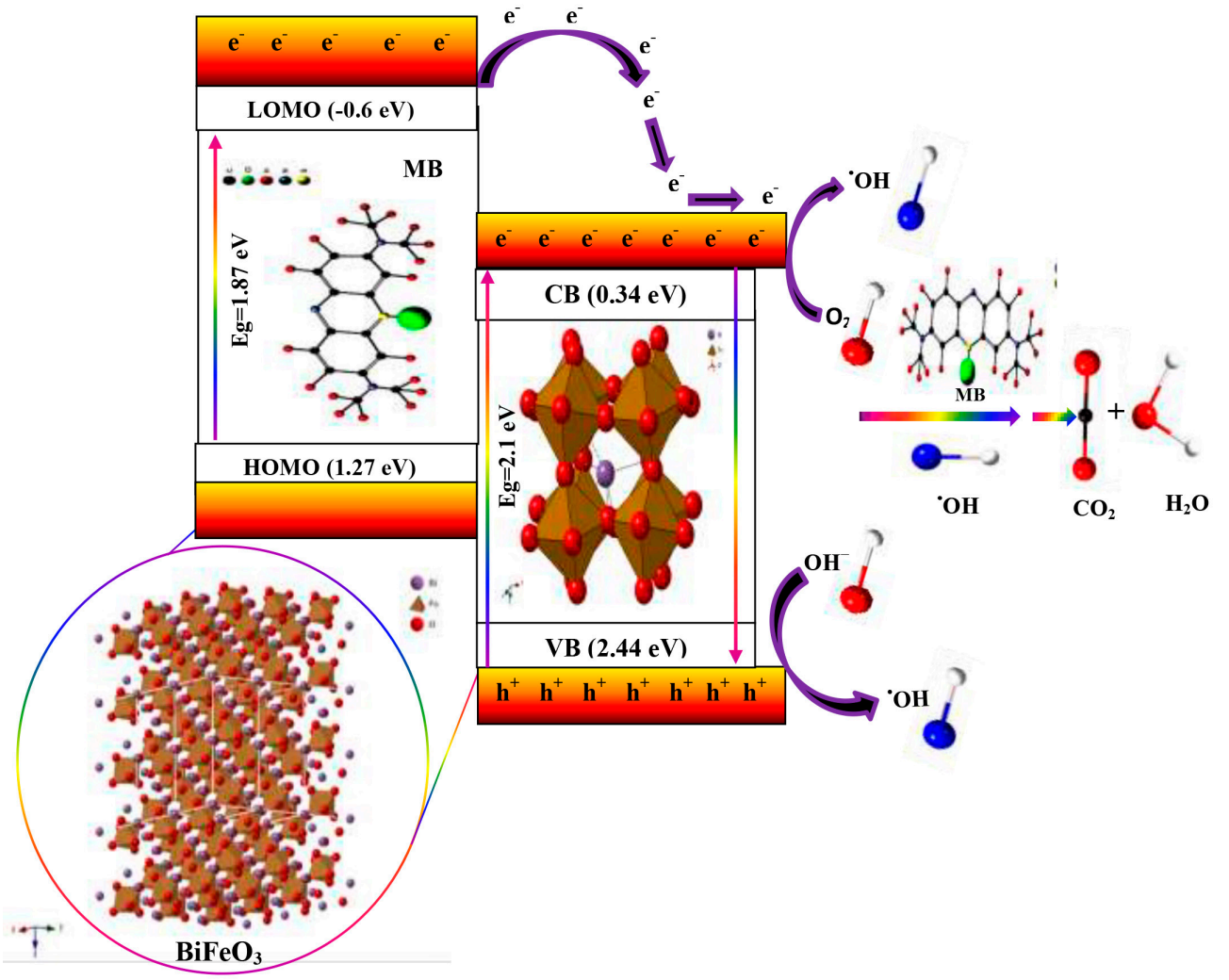

Figure 10: Proposed mechanism of photocatalytic degradation of MB over BFO-600 after adsorption of MB under the LED-50 W irradiation.

$$MB + {}^{\bullet}OH \rightarrow \text{intermediates} \rightarrow CO_2 + H_2O \quad (AC)$$

The dye-sensitization process is a crucial step for the photocatalytic reaction under LED 50 W light exposure because the dye molecule can provide more electrons to perovskite photocatalyst via the photo-irradiation process. The dye molecule has a double character: as a molecular bridge, it attaches semiconductor photocatalyst with an electron donor and, as a sensitizer, it absorbs visible light. There are a few other parameters that are equally important in the dye-sensitization process: i) the energy level compatibility between the excited sensitizer and the conduction band of the semiconductor; and ii) redox potential of the dye/dye^{+} couple, and stability of the dye to undergo about 10^8 turnover cycles. Methylene blue (MB) is a blue cationic thiazine dye with λ_{max} value at 664 nm, which originates from the $\pi \rightarrow \pi^*$ transitions from the binding HOMO (highest occupied molecular orbital) to the anti-binding LUMO (lowest unoccupied molecular orbital). However, the shoulder around 521 nm is usually ascribed to the dimmer. The bands below 450 nm represent the transitions to the mesomeric limit structures in which the positive charge can be placed either on the amine nitrogen atom or on the sulfur atom with shorter conjugation units and originate from $n \rightarrow \pi^*$ transitions from the NHOMO (next highest occupied molecular orbital) to the LUMO. The reduced forms of MB, leuco-methylene blue (LMB) (λ_{max}=256 nm) [45] and MBH^{2+} (λ_{max}=232 nm) [46] are colorless and stable in aqueous solution. MB is blue in an oxidizing environment and readily reduced to the colorless, leuco forms by reducing agents [47].

According to the UV-vis-DRS results, both BFO-600 catalyst and MB dye, which are only stimulated by visible irradiation, absorb at 590.47 nm (E_g=2.1 eV) and 664 nm (E_g=1.87 eV), respectively. Upon irradiation by LED 50 W lamp, the electrons (e^-) in the VB of the BFO-600 NPs get

Table V - $BiFeO_3$ nanoparticles as photocatalyst of methylene blue dye.

Synthesis route	Size and shape	Bandgap (eV)	Experimental conditions	Fraction of dye degradation	Ref.
Ultrasound	40.12 nm	2.17	1.5 mg.L^{-1} MB, 0.5 g.L^{-1} PC, sunlight	100% after 90 min	[39]
Sol-gel	128 nm	2.324 ±0.013	1 mg.L^{-1} dye, 5 mg.L^{-1} PC, 500 W Xe lamp	68% after 50 min	[41]
Solvothermal	Microsphere	2.1	10 mg.L^{-1} dye, 50 mg.L^{-1} PC, 500 W Xe lamp	86% after 240 min	[42]
Sol-gel	100 nm	1.6	20 mg.L^{-1} dye, 2.5 g.L^{-1} PC, 300 W Xe lamp	98% after 240 min	[48]
Biotemplate method	14.76 nm	-	10 mg.L^{-1} dye, 12.79 mmol.L^{-1}, sunlight	96% after 180 min	[43]
Co-precipitation	Nanocrystalline	2.06	10 mg.L^{-1} dye, 0.5 g.L^{-1} PC, 300 W Xe lamp	40% after 30 min	[49]
Sol-gel	60 nm	2.1	100 mg.L^{-1} dye, 1 g.L^{-1} PC, 300 W Xe lamp$^{\#}$, 5 W LED*	$^{\#}$40% after 180 min, *35% after 180 min	[50]
Hydrothermal	Submicron cube	2.90	40 mg.L^{-1} dye, 2.5 g.L^{-1} PC, 150 W Xe lamp	10% in 140 min	[51]
Sol-gel	24 nm	2.00	10 mg.L^{-1} dye, 1 g.L^{-1}, sunlight	76% in 9 h	[52]
Glyoxylate precursor method	23.6 nm	2.17	15 mg.L^{-1} dye, 1 g.L^{-1} PC, 100 W Xe lamp	94.5% in 120 min	[53]
Thermal decomposition of glyoxylate precursor	52 nm	2.10	10 mg.L^{-1} dye, 1 g.L^{-1} PC, sunlight	61% in 90 min	[54]
Sol-gel	Nanocrystalline	2.2	20 mg.L^{-1} dye, 0.25 g.L^{-1} PC, 500 W Xe lamp	34%	[55]
High-energy ball milling	176 nm	2.2	10 mg.L^{-1} dye, 0.5 g.L^{-1} PC, 500 W halogen W lamp	94% in 120 min	[56]
Co-precipitation	24.4 nm	2.1	10 mg.L^{-1} dye, 0.5 g.L^{-1} PC, 50 W LED	94.4% in 120 min	Present work

excited and jump onto the CB with simultaneous generation of the same amount of holes (h^+) in the VB. Meanwhile, cationic organic dye molecules (MB^+) were adsorbed on the surface of the BFO-600, and then the electrons in adsorbed MB-homo (+1.27 V/NHE) were excited to generate the excited electrons. The electrons in MB*-LUMO (-0.6 V/NHE, Eq. AD) were injected into CB of BFO-600 (+0.34 eV/NHE), due to the more positive energy level of the CB of BFO-600, compared with LUMO state of MB*, generating dye cationic radical $MB^{\bullet+}$ (Eq. AE). The photo-excited electron on the CB of BFO-600 could reduce the dissolved O_2 to $^{\bullet}OH$ as mentioned in Eq. AF. Then, the oxidation of MB by $^{\bullet}OH$ radical (Eq. AG) and h^+_{VB} (Eq. AH) took place to degrade MB to smaller molecules. Based on the above results, the proposed mechanism of dye-sensitized BFO-600 photocatalyst under the LED 50 W light irradiation is as follows:

$$MB@BFO\text{-}600 + h\nu_{(LED\text{-}50W)} \rightarrow MB^*@BFO\text{-}600(e^-_{CB} + h^+_{VB}) \quad (AD)$$

$$MB^*@BFO\text{-}600(e^-_{CB} + h^+_{VB}) \rightarrow MB^{\bullet+}@BFO\text{-}600(e^-_{CB} + h^+_{VB}) \quad (AE)$$

$$O_2 + 2H_2O + BFO\text{-}600\ (4e^-_{CB}) \rightarrow 4^{\bullet}OH \quad (AF)$$

$$MB_{ads} + {}^{\bullet}OH \rightarrow intermediates \rightarrow CO_2 + H_2O \quad (AG)$$

$$MB_{ads} + h^+_{VB} \rightarrow intermediates \rightarrow CO_2 + H_2O \quad (AH)$$

Under white LED-50 W irradiations and at basic aqueous solutions (pH=11), highly reactive hydroxyl radicals can be formed through monoelectronic reduction of MB^+ by the hydroxyl ion [48]:

$$MB^+ + OH^- + h\nu_{(LED\text{-}50W)} \rightarrow MB^{\bullet} + {}^{\bullet}OH \quad (AI)$$

and $^{\bullet}OH$ radicals can react with each other and produce H_2O_2, which is an important active species in degradation processes:

$$2^{\bullet}OH \rightarrow H_2O_2 \quad (AJ)$$

Adsorbed oxygen acting as a radical scavenger can react with $MB^{\bullet}$ radical and form $O_2^{-\bullet}$ as another important intermediate species according to the reaction [49]:

$$MB^{\bullet} + O_2 \rightarrow MB^+ + O_2^- \quad (AK)$$

Finally, all generated active radicals are able to decompose MB molecules via successive attack by h^+_{VB}, $^{\bullet}OH_{ads}$, H_2O_2, and $MB^{\bullet+}_{ads}$ active species into intermediates or mineralized products:

$$MB + (h^+; {}^{\bullet}OH_{ads}, H_2O_2, MB^{\bullet+}_{ads}) \rightarrow intermediates \rightarrow CO_2 + H_2O \quad (AL)$$

The degradation of MB could be preceded via dye sensitization process under white LED-50 W irradiations, as an efficient method to enhance the photoresponse of BFO-600 NPs in the visible range and has been effectively used for environmental applications. Fig. 10 shows the schematic diagram of the dye-sensitized BFO-600 photocatalyst under the 50 W LED light irradiation. The comparison of various synthesis techniques and experimental operating conditions on the photocatalytic performance of the $BiFeO_3$ catalyst towards methylene blue dye was established, from the elaboration, characterization, and application of $BiFeO_3$ micro-particles in the photocatalysis degradation of methylene blue, as probe dye, under LED irradiation. $BiFeO_3$ micro-particles, synthesized via co-precipitation route, seem to have the best compromise among the synthesis techniques reviewed, as displayed in Table V.

CONCLUSIONS

$BiFeO_3$-NPs were successfully synthesized via a coprecipitation-calcination method and characterized by TGA, XRD, SEM-EDX, and UV-vis-DRS techniques. The photocatalytic efficiency of the as-prepared $BiFeO_3$ catalyst was assessed for the first time using white LED-light-initiated degradation of methylene blue (MB) at various experimental key parameters (pH of solution, catalyst dosage, initial concentration of dye, and calcination temperature). Results showed that BFO-600 (sample calcined at 600 °C) was a rhombohedrally-distorted perovskite oxide with the R3c space group. The average crystal size and band gap energy for BFO-600 were found to be 24.8 nm and 2.1 eV, respectively. Under optimal operating conditions ([MB]=20 $mg.L^{-1}$, BFO-600/dye mass ratio=0.5 $g.L^{-1}$, pH=11, and 25 °C), MB/BFO-600/LED process exhibited an efficient photodegradation (up to 94.4%) within 120 min under white LED irradiation, much higher than the MB sorption process (MB/BFO-600/dark system, 69.4%) and the MB self-photolysis system (MB/LED, 33.9%). The photocatalytic degradation of MB was found to fit well with the pseudo-first-order kinetic model. Thus, the MB photodegradation was attributed to the generation of reactive radicals such as $^{\bullet}OH$, h^+, H_2O_2, and $MB^{\bullet+}$ via direct heterogeneous photocatalysis and mediated by MB through a self-photosensitization process of MB over BFO-600 NPs.

ACKNOWLEDGMENT

The work is supported by the University of Sciences and Technology of Oran, Algeria.

REFERENCES

[1] G. Zhang, G. Liu, L. Wang, J.T.S. Irvine, Chem. Soc. Rev. **45** (2016) 5951.
[2] L. Di, H. Yang, T, Xian, X, Liu, X. Chen, Nanomaterials **9** (2019) 1.
[3] J. Wang, J.B. Neaton, H. Zheng, V. Nagarajan, S.B. Ogale, B. Liu, D. Viehland, V. Vaithyanathan, D.G. Schlom, U.V. Waghmare, N.A. Spaldin, K.M. Rabe, M. Wutting, Science **299** (2003) 1719.
[4] M. Fiebig, T. Lottermoser, D. Frohlich, A.V. Goltsev, R.V. Pisarev, Nature **419** (2002) 818.

[5] M.M. Kumar, V.R. Palkar, K. Shrinivas, S.V. Suryanarayan, Appl. Phys. Lett. **76** (2000) 2764.
[6] A. Srinivas, D.W. Kim, K.S. Hong, S.V. Suryanaraynan, Appl. Phys. Lett. **83** (2003) 2217.
[7] H. Liu, Z. Liu, Q. Liu, K. Yao, Thin Solid Films **500** (2006) 105.
[8] F. Kubel, H. Schmid, Acta Cryst. B **46** (1990) 698.
[9] X. Xu, Y.H. Lin, P. Li, L. Shu, C.W. Nan, J. Am. Ceram. Soc. **94** (2011) 2296.
[10] Z.L. Hou, H.F. Zhou, J. Yuan, Kang, H.J. Yang, H.B. Jin, M.S. Cao, Chin. Phys. Lett. **28** (2011) 37702.
[11] M.Y. Shami, M.S. Awan, M.A. Rehman, J. Alloys Compd. **509** (2011) 10139.
[12] J.H. Xu, H. Ke, D.C. Jia, W. Wang, Y. Zhou, J. Alloys Compd. **472** (2009) 477.
[13] N. Das, R. Majumdar, A. Sen, H.S. Maiti, Mater. Lett. **61** (2007) 2100.
[14] J. Yang, X. Li, J. Zhou, Y. Tang, Y. Zhang, Y. Li, J. Alloys Compd. **509** (2011) 9271.
[15] Y. Liu, Q. Qian, Z. Yi, L. Zhang, F. Min, M. Zhang, Ceram. Int. **39** (2013) 8513.
[16] S. Farhadi, N. Rashidi, Polyhedron **29** (2010) 2959.
[17] J.K. Kim, S.S. Kim, W.J. Kim, Mater. Lett. **59** (2005) 4006.
[18] J.H. Xu, H. Ke, D.C. Jia, W. Wang, Y. Zhou, J. Alloys Compd. **472** (2009) 473.
[19] J. Wang, Y. Wei, J. Zhang, L. Ji, Y. Huang, Z. Chen, Mater. Lett. **124** (2014) 242.
[20] O. Sacco, M. Stoller, V. Vaiano, P. Ciambelli, A. Chianese, D. Sannino, Int. J. Photoenergy **2012** (2012) 8.
[21] T.D. Nguyen, V.D. Cao, L.X. Nong, V.H. Nguyen, L.G. Bach, N.T.H. Le, T.D. Luu, S.S. Hong, K.T. Lim, DV.N. Vo, ChemistrySelect **4** *(*2019) 6048.
[22] S. Balu, K. Uma, G.T. Pan, T.C.K. Yang, S.K. Ramaraj, Materials **11** (2018) 1030.
[23] A. Habibi-Yangjeh, M. Shekofteh-Gohari, Prog. Nat. Sci. **29** (2019) 145.
[24] D. Wu, W. Wang, T.W. Ng, G. Huang, D. Xia, H.Y. Yip, H.K. Lee, G. Li, T. And, P.K. Wong, J. Mater. Chem. A **4** (2016) 1052.
[25] K. Sarkar, "Synthesis, characterization and property evaluation of Ni and Co doped bismuth ferrite multiferroic materials", Master Thesis, Jadavpur Un. Kolkata, India (2011).
[26] B.D. Cullity, *Elements of X-ray diffraction*, 2nd ed., Addison-Wesley, Massachusetts (1978).
[27] J. Zhang, L. Gao, J. Solid State Chem. **177** (2004) 1425.
[28] A.A. Hoseini, S. Farhadi, A. Zabardasti, F. Siadatnasab, RSC Adv. **9** (2019) 24489.
[29] K. Sattler, in "Handbook of thin films materials: 5 nanomaterials and magnetic thin films", H.S. Nalwa (Ed.), Acad. Press, New York (2002) 61.
[30] X. Bai, "Size and doping effect on the structure, transitions and optical properties of multiferroic $BiFeO_3$ particles for photocatalytic applications", Dr. Thesis, Un. Paris-Saclay, France (2016).
[31] B. Jansi Rani, G. Ravi, R. Yuvakkumar, M. Thambidurai, J. Sol-Gel Sci. Technol. **91** (2019) 247.
[32] R. Palai, R. Katiyar, H. Schmid, P. Tissot, S. Clark, J. Robertson, S. Redfern, G. Catalan, J.B. Scott, Phys. Rev. B **77** (2008) 14110.
[33] N. Laouedj A. Elaziouti, N. Benhadria, A. Bekka, J. Rare Earths **36** (2018) 575.
[34] S. Valencia, J.M. Marin, G. Restrepo, Open Mater. Sci. J. **4** (2010) 9.
[35] C. He, C. Deng, J. Wang, X. Gu, T. Wu, K. Zhu, Y. Liu, Phys. B Cond. Matt. **483** (2016) 44.
[36] F. Gao, X. Chen, K. Yin, S. Dong, Z. Ren, F. Yuan, T. Yu, Z. Zou, J.-M. Liu, Adv. Mater. **19** (2007) 2889.
[37] M.R. Gholipour, C.T. Dhin, F. Béland, T.O. Do, Nanoscale **7** (2015) 8187.
[38] A. Elaziouti, N. Laouedj, J. Kor. Chem. Soc. **54** *(*2010) 300.
[39] T. Soltani, M.H. Entezar, Ultrason. Sonochem. **20** (2013) 1245.
[40] C. Ponraj, G. Vinitha, D. Joseph, Environ. Nanotechnol. Monit. Manag. **7** (2017) 110.
[41] S. Bharathkumar, M. Sakar, S. Balakumar, J. Phys. Chem. C **120** (2016) 18811.
[42] Y. Huo, Y. Jin, Y. Zhang, J. Mol. Catal. A Chem. **331** (2010) 15.
[43] H.A.M. Azmy, N.A. Razuki, A.W. Aziz, N.S. Abdul Satar, N.H.M. Kaus, J. Phys. Sci. **28** (2017) 85.
[44] A. Khataee, V. Vatanpour, A.A. Ghadim, J. Hazard. Mater. **161** (2009) 1225.
[45] H. Obata, Bull. Chem. Soc. Jpn. **34** (1961) 1057.
[46] A. Mills, J. Wang, J. Photochem. Photobiol. A Chem. **127** (1999) 123.
[47] T. Snehalatha, K.C. Rajanna, P.K. Saoprakash, J. Chem. Educ. **74** (1997) 228.
[48] H. Huo, X. Hu, H. Wang, J. Li, G. Xie, X. Tan, Q. Jin, D. Zhou, C. Li, G. Qiu, Y. Liu, Int. J. Environ. Res. Public Health **16** (2019) 3219.
[49] S. Jiao, Y. Zhao, C. Li, B. Wang, Q. Yang, Green Energy Environ. **4** (2019) 66.
[50] S. Irfan, S. Rizwan, Y. Shen, L. Li, Asfandiyar, S. Butt, C.W. Nan, Sci. Rep. **7** (2017) 42493.
[51] J. Li, Y. Wang, H. Ling, Y. Qiu, J. Lou, X. Hou, S.P. Bag, J. Wang, H. Wu, G. Chai, Nanomaterials **9** (2019) 1.
[52] Y. Subramanian, V. Ramasamy, R.J. Karthikeyan, G.R. Srinivasan, D. Arulmozhi, R.K. Gubendiran, M. Sriramalu, Heliyon **5** (2019) e01831.
[53] B. Safizade, S.M. Masoudpanah, M. Hasheminiasari, A. Ghasemi, RSC Adv. **8** (2018) 6988.
[54] S.M. Masoudpanah, S.M. Mirkazemi, J. Nanostruct. **7** (2017) 183.
[55] Y.H. Si, Y. Xia, S.K. Shang, X.B. Xiong, X.R. Zeng, J. Zhou, Y.Y. Li, Nanomaterials **8** (2018) 526.
[56] E.A. Volnistem, R.D. Bini, G.S. Dias, L.F. Cótica, I.A. Santos, Ferroelectrics **534** (2018) 190.
(Rec. 21/05/2021, Rev. 23/07/2021, 18/09/2021, Ac. 22/09/2021)